Bol. Soc. Paran. Mat.
©SPM – E-ISSN-2175-1188
SPM: www.spm.uem.br/bspm

(3s.) **v. 2026 (44) 2** : 1–19.
ISSN-0037-8712
doi:10.5269/bspm.78975

Numerical Simulation of Water Sloshing in Rectangular Tank Using Virtual Source Method

Omar Al-Tameemi, A. Al-Sabbagh, Ruaa Wana and Aqeel Jassim Noor

ABSTRACT: This study investigates two-dimensional sloshing in a stationary rectangular tank initiated by a tilt-and-release free surface, simulated using the Virtual Source Method (VSM). The motivation arises from the need for fast, accurate potential-flow solvers for sloshing phenomena relevant to marine, aerospace, and civil applications. The inviscid, irrotational formulation represents the potential through rectangular-domain eigenfunctions with a closed-form vertical kernel, while time derivatives are obtained from an over-determined least-squares system and advanced with a classical fourth-order Runge–Kutta scheme. The VSM achieves fourth-order temporal convergence and approximately second-order spatial convergence of global invariants (energy, volume) across tilt amplitudes. Long-time integrations remain conservative and stable, exhibiting negligible volume drift and bounded energy variation. These results demonstrate that VSM provides a compact, efficient, and high-fidelity framework for nonlinear sloshing analysis in rectangular tanks.

Keywords: Virtual Source Method, Energy Conservation, Numerical Sloshing Tank.

Contents

1. Introduction

The study of liquid sloshing in partially filled containers has long been of practical importance in ocean, coastal, aerospace, and civil engineering applications. Typical scenarios include sloshing in ship ballast tanks, cargo carriers, offshore platforms, and propellant tanks of spacecraft, as well as water storage reservoirs subjected to seismic excitation. The free-surface oscillations that arise in such systems can generate significant hydrodynamic loads on the tank walls and may couple strongly with the structural motion of the container. Under resonant excitation, the sloshing motion becomes highly nonlinear, often leading to wave breaking, impact pressures, and violent free-surface deformation. Accurate prediction of these phenomena is therefore essential for the safe design and operation of engineering systems [1].

A wide variety of theoretical, numerical, and experimental approaches have been developed to investigate liquid sloshing. Analytical studies, particularly for small-amplitude oscillations, provide valuable insights into natural frequencies and modal characteristics of rectangular and cylindrical tanks [2]. However, such linear or weakly nonlinear theories are unable to capture strongly nonlinear behaviors, such as steep free-surface deformations, secondary resonance, and overturning waves. To address these limitations, computational methods have been widely applied.

2020 *Mathematics Subject Classification:* 37N30, 65M38.
Submitted September 15, 2025. Published March 14, 2026

Computational fluid dynamics (CFD) models that solve the full Navier-Stokes equations have become increasingly popular for sloshing studies. Techniques such as the volume-of-fluid (VOF) method, marker-and-cell (MAC) method, Cartesian cut-cell finite volumes, and particle methods (e.g., SPH/MPS) have been employed to simulate violent free-surface flows including wave breaking, splashing, and fluid-structure interaction [3,4,7,8,5].

Recent research demonstrates that a smoothed particle hydrodynamics method with adaptive spatial resolution (SPH-ASR)—which refines particle distribution near the free surface and dynamic boundaries—precisely replicates violent sloshing (including significant deformation and fragmentation), validated against standard experiments, and delineates the dependence of loads on fill level, forcing frequency, and amplitude in prismatic and rectangular tanks [6].

While these models provide detailed descriptions of viscous and turbulent effects, they are computationally expensive, particularly for three-dimensional simulations and long-duration sloshing events. This computational cost often limits their use in parametric studies and engineering design applications.

Potential-flow models, in which the velocity field is represented by a velocity potential satisfying Laplace's equation, offer a more efficient alternative for many sloshing problems where viscous effects are secondary. Within this framework, several numerical techniques have been developed. The mixed Eulerian–Lagrangian (MEL) method introduced by [15] has been widely used to track the evolution of nonlinear free surfaces, while [9] applied the finite element method to the nonlinear potential-flow formulation. The boundary element method (BEM) has been particularly popular in sloshing and wave-tank simulations [10,11,2]. By reformulating Laplace's equation as a boundary integral equation, BEM reduces the problem dimension by one and allows efficient handling of large free-surface deformations. Nevertheless, BEM suffers from several drawbacks: it requires the discretization of the entire boundary at every time step, often leading to large dense linear systems; it can lose accuracy for long-time integration; and it is prone to numerical instability in strongly nonlinear regimes. Recent studies underscore both the complexity of sloshing near critical fillings and the need for efficient, high-order solvers and diagnostics, spanning experimental, numerical and analytical advances [18,19,20,21,22].

In recent years, the *Virtual Source Method* (VSM) proposed by [12] has emerged as a promising alternative for nonlinear free-surface potential-flow simulations. The VSM is based on Green's identity with specially chosen Green's functions corresponding to a rectangular "virtual domain." This formulation allows the velocity potential and its spatial derivatives to be expressed analytically as Fourier-type expansions, thereby eliminating the need for boundary discretization within the physical domain. As a result, VSM provides a mesh-free evaluation of velocities and pressures in the fluid, and avoids some of the numerical instabilities that can affect BEM.

The effectiveness of VSM has been demonstrated in several recent studies. [13] applied the method to simulate nonlinear standing waves, highlighting its superior performance compared with BEM in terms of energy and volume conservation, convergence rates, and computational efficiency. The method was subsequently extended to progressive-wave simulations by [14], where artificial damping layers were introduced to reduce wave reflection, and the numerical results were validated against second-order Stokes theory and experimental data. These studies confirmed that VSM is both accurate and stable for long-term integration, and that it offers significant computational savings relative to BEM (see also [16] for a broader review of numerical wave modelling).

Building on these developments, Langfeld et al. [12] first demonstrated the capability of the Virtual Source Method (VSM) for modelling sloshing dynamics in two-dimensional tanks, while Al-Tameemi et al. [13] investigated its stability and conservation characteristics, confirming the method's ability to preserve mass and energy over long integrations. Nevertheless, the comprehensive application of VSM to *sloshing flows in partially filled tanks*—where container geometry, initial tilt, and nonlinear free-surface motion interact—has not yet been systematically analysed. Sloshing differs fundamentally from standing or progressive waves in that the container motion or initial tilt provides the driving mechanism for the free-surface oscillations. This introduces additional complexities such as coupling between tank geometry and fluid acceleration, resonance amplification, and highly nonlinear free-surface deformation, along with intricate pressure distributions on the tank walls that are directly relevant to structural design. Accurately capturing these dynamics while maintaining numerical stability and efficiency over long simulations remains a challenge for conventional numerical approaches.

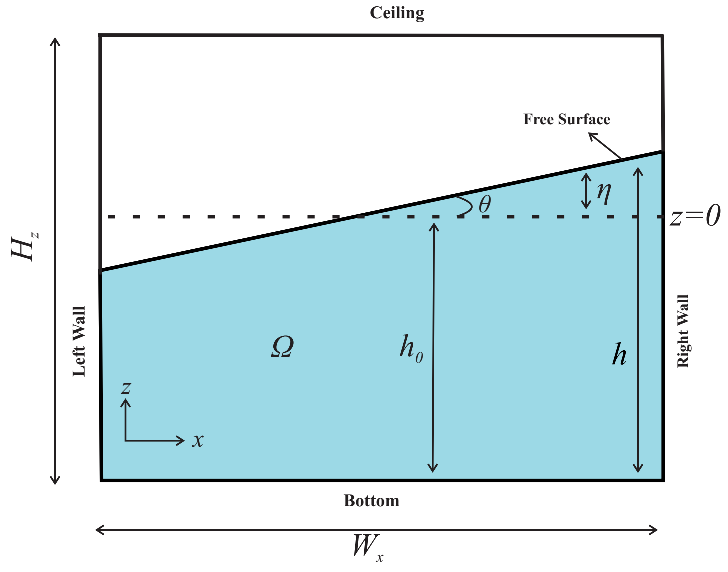

Figure 1: Schematic of the rectangular sloshing tank, coordinate system, and boundary notation.

The present study extends the VSM framework to provide a full analysis of two-dimensional sloshing in rectangular tanks. The main objectives are: (i) to examine the accuracy of VSM in predicting free-surface elevations and hydrodynamic responses under different initial tilts; (ii) to quantify the conservation of total energy and volume as measures of numerical robustness; and (iii) to benchmark the method's convergence behaviour against analytical solutions. Through this extension, we demonstrate that the VSM preserves its intrinsic advantages of accuracy, stability, and efficiency when applied to the complex and practically significant problem of nonlinear sloshing.

2. Governing Equations and Tank Geometry

We consider a two-dimensional, partially filled rectangular tank of width W_x and still-water depth h_0. A right-handed Cartesian coordinate system (x, z) is adopted with the x-axis horizontal and the z-axis vertical and positive upwards. The calm free-surface level is at $z = 0$, the bottom is at $z = -h_0$, and the rigid vertical walls are at $x = 0$ and $x = W_x$. The instantaneous free-surface elevation is denoted by $z = \eta(x, t)$ (Figure 1). The container is fixed in space; no imposed wall motion or external excitation is applied.

The liquid is assumed inviscid, incompressible, and irrotational. Hence, the velocity field is given by $\boldsymbol{u} = \nabla\varphi(x, z, t)$ for a velocity potential $\varphi(x, z, t)$ that satisfies Laplace's equation in the time-dependent fluid domain $\Omega(t)$:

$$\nabla^2\varphi \;=\; \frac{\partial^2\varphi}{\partial x^2} + \frac{\partial^2\varphi}{\partial z^2} \;=\; 0 \quad \text{in } \Omega(t). \tag{2.1}$$

On the free surface $z = \eta(x, t)$, the kinematic boundary condition (material impermeability) is

$$\frac{\partial\eta}{\partial t} \;=\; \frac{\partial\varphi}{\partial z} \;-\; \frac{\partial\varphi}{\partial x}\,\frac{\partial\eta}{\partial x} \quad \text{on } z = \eta(x, t), \tag{2.2}$$

and the dynamic boundary condition (unsteady Bernoulli with atmospheric pressure on the interface) is

$$\frac{\partial\varphi}{\partial t} \;=\; -\,g\,\eta \;-\; \tfrac{1}{2}\,|\nabla\varphi|^2 \quad \text{on } z = \eta(x, t), \tag{2.3}$$

where g is the gravitational acceleration. The rigid walls and bottom are impermeable,

$$\frac{\partial\varphi}{\partial n} \;=\; 0 \quad \text{on } \Gamma_s \equiv \{x = 0\} \cup \{x = W_x\} \cup \{z = -h_0\}. \tag{2.4}$$

In this study, sloshing is initiated solely by a prescribed initial condition that encodes an overall free-surface tilt of angle θ (Figure 1), after which the fluid is released from rest in a fixed tank.

3. Virtual Source Method

The fundamental concept of the VSM is to substitute the free-space solution of Laplace's equation within the computing domain with a virtual rectangular wave tank, where the upper boundary accommodates the solution degrees of freedom. The degrees of freedom are the time-dependent Fourier coefficients $\{\zeta_n(t)\}_{n\geq 1}$ of $\varphi(x,z,t)$ at the upper boundary. For a given $\zeta_n(t)$, the potential $\varphi(\cdot,t)$ and its spatial derivatives are expressed in closed form throughout the tank. The free-surface conditions yield an overdetermined ordinary differential equation system for $\dot{\zeta}_n(t)$, which is completed by the kinematic update of $\eta(x,t)$.

The VSM was initially introduced by Langfeld et al. (2016), who examined Laplace's equation (2.1) about the standing wave issue. They defined dimensionless quantities of variables by assigning the tank width W_x and height H_z as the primary units of length as follows [12]:

$$x = W_x\,\bar{x}, \qquad z = H_z\,\bar{z}, \tag{3.1}$$

The non-dimensional quantities for u, v, $\varphi(x,z,t)$, and t are defined as follows:

$$\begin{aligned} u &= \sqrt{g\,H_z}\tfrac{H_z}{W_x}\bar{u}, \qquad & v &= \sqrt{g\,H_z}\bar{v} \\ \varphi &= \sqrt{g\,H_z{}^3}\,\bar{\varphi}\,, \qquad & t &= \sqrt{H_z/g}\bar{t} \end{aligned} \tag{3.2}$$

Ultimately, the kinematic and dynamic boundary conditions of the free surface (2.3) and (2.2) are expressed as follows:

$$\frac{\partial\bar{\varphi}}{\partial\bar{t}} = -\bar{z} - \frac{1}{2}\,,\left[\gamma^2\bar{u}^2 + \bar{v}^2\right], \qquad \text{on } z=\eta, \tag{3.3}$$

$$\frac{\partial\bar{h}}{\partial\bar{t}} = -\gamma^2\bar{u}\frac{\partial\bar{h}}{\partial\bar{x}} + \bar{v}(\mathbf{x},t), \qquad \text{on } z=\eta, \tag{3.4}$$

where $\gamma = \frac{H_z}{W_x}$.

The function $\varphi(x,t)$ can be represented in the subsequent equation

$$\varphi(\mathbf{x},t) = \sum_{n\in\mathbb{N}} \zeta_n(t)\cos(\kappa_n x) F\left(\gamma n,\, \frac{z}{H_z}\right), \tag{3.5}$$

where $\zeta_n(t)$ represents the n^{th} component of the Fourier cosine transform of $\varphi(x,z,t)$ along the ceiling, and $\kappa_n = \frac{n\pi}{W_x}$.

$$F(\kappa,\bar{z}) = \sum_{\nu=0}^{\infty}(-1)^{\nu}\left[\mathrm{e}^{-\pi\kappa(2\nu+1+\bar{z})} + \mathrm{e}^{-\pi\kappa(2\nu+1-\bar{z})}\right], \kappa > 0. \tag{3.6}$$

The function F comprises an alternating sum with terms that diminish fast. Consequently, it may be assessed computationally in a swift and dependable manner.

The infinite sum (3.5) is substituted with a finite sum consisting of a restricted number of frequency components M_c in order to determine $\varphi(\mathbf{x},t)$ and free surface components in the following way:

$$\varphi(\mathbf{x},t) \approx \sum_{n=1}^{M_c} \zeta_n(t)\cos(\kappa_n x) F\left(\gamma n,\, \frac{z}{H_z}\right). \tag{3.7}$$

The equation above may be used to analytically determine the velocity components at each mesh-free spatial and temporal point

$$\nabla\varphi(\mathbf{x},t) \approx \sum_{n=1}^{M_c} \zeta_n(t)\nabla\left[\cos(\kappa_n x) F\left(\gamma n,\, \frac{z}{H_z}\right)\right]. \tag{3.8}$$

Then,

$$u(\mathbf{x},t) \approx -\sum_{n=1}^{M_c} \zeta_n(t)\, \kappa_n \cos(\kappa_n x) F\left(\gamma n,\, \frac{z}{H_z}\right), \tag{3.9}$$

$$v(\mathbf{x},t) \approx \sum_{n=1}^{M_c} \zeta_n(t)\, \cos(\kappa_n x)\, \frac{\partial F}{\partial z}\left(\gamma n,\, \frac{z}{H_z}\right). \tag{3.10}$$

The dimensionless dynamic boundary condition 2.3 can now be articulated as:

$$\frac{\partial \bar{\varphi}}{\partial \bar{t}} = -\bar{z} - \frac{1}{2}\,, \left[\gamma^2 \bar{u}^2 + \bar{v}^2\right] = B\left(\bar{\mathbf{x}}, \eta(\bar{x},\bar{t}), \zeta_n(\bar{t})\right) \qquad \text{on } z = \eta. \tag{3.11}$$

Hence,

$$\sum_{n=1}^{M_c} \frac{d\zeta_n(\bar{t})}{d\bar{t}} \cos(\kappa_n \bar{x}) F\left(\gamma n, \bar{z}\right) = B(\bar{\mathbf{x}}, \eta(\bar{\mathbf{x}}, \bar{t}), \zeta_n(\bar{t})). \tag{3.12}$$

To compute $\frac{d\zeta_n(\bar{t})}{d\bar{t}}$, select a collection of resolution points M_x, where $M_x > M_c$, then:

$$\sum_{n=1}^{M_c} \frac{d\zeta_n(\bar{t})}{d\bar{t}} \cos(\kappa_n \bar{x}_i) F\left(\gamma n, \bar{z}\right) = B(\bar{\mathbf{x}}_i, \eta(\bar{\mathbf{x}}_i, \bar{t}), \zeta_n(\bar{t})), \;\; i = 1, \ldots M_x. \tag{3.13}$$

Here, the resolution points M_x denote the number of discrete collocation positions along the free surface where the kinematic and dynamic conditions are enforced. Increasing refines the spatial representation of the surface modes and directly controls the spatial accuracy of the least-squares system. In order to find the time derivative of $\zeta_n(t)$, the final equation generates an overdetermined linear system. Using least squares, this research solves the given issue and then determines $\zeta_n(t)$ by applying Runge-Kutta 4 integration. However, computing the time derivative $d\eta/dt$ is required for Runge-Kutta integration. To analytically compute the free surface elevation.

$$\bar{h}(\bar{x},\bar{t}) = \sum_{k=0}^{N_A} [a_k(\bar{t}) \cos(\frac{2\pi}{W_x} k\, \bar{x}) + b_k(\bar{t}) \sin(\frac{2\pi}{W_x} k\, \bar{x})], \tag{3.14}$$

N_A denotes the quantity of frequency components. The analytical calculation of the spatial derivative yields the following equation, which reflects the *Airy mode decomposition*:

$$\frac{\partial}{\partial \bar{x}} \bar{z}(\bar{x},\bar{t}) = \sum_{k=0}^{N_A} [-k a_k(\bar{t}) \sin(\frac{2\pi}{W_x} k\, \bar{x}) + k b_k(\bar{t}) \cos(\frac{2\pi}{W_x} k\, \bar{x})] = A\left(\bar{x}, a_k(\bar{t}), b_k(\bar{t})\right). \tag{3.15}$$

Consequently, from equations (3.4), (3.9), (3.10), (3.14), and (3.15), one may derive,

$$\sum_{k=0}^{N_A} [\frac{da_k(t)}{dt} \cos(\frac{2\pi}{W_x} k\, x) + \frac{db_k(t)}{dt} \sin(\frac{2\pi}{W_x} k\, x)] = -\gamma^2\, \bar{u}\, A\left(\bar{x}, a_k(\bar{t}), b_k(\bar{t})\right) + \bar{v}$$

$$= H\left(\bar{x}, a_k(\bar{t}), b_k(\bar{t}), \zeta_n(t)\right) \tag{3.16}$$

Similarly, choose a collection of $N_s \geq 2N_A$ points for $\bar{x}$ by computing $d\zeta_n(t)/dt$; hence, the overdetermined system may be treated once again using least squares. Now, at time t, $\zeta_n(t)$, and $a(t)$, $b(t)$ are the results of the Runge-Kutta 4 integration.

4. Numerical Setup and Results

4.1. Numerical Tank Setup

We simulate sloshing from a tilt-and-release initial condition in a fixed rectangular tank ($W_x = 2$ m, $H_z = 1.5$ m, $h_0 = 1$ m) using the VSM. Neglecting the viscous and nonlinear effects, the linear analytical solution for free surface elevation can be approximated using linear wave theory, which expresses interface displacement as a function of x, t and θ as follows [17].

$$\eta(x,t) = \sum_{n=1}^{\infty} \frac{4\tan\theta}{n^2\pi^2} W_x \sin\left(\frac{n\pi}{2}\right) \sin(\kappa_n x) \cos(\omega_n t), \tag{4.1}$$

where $\kappa_n = \frac{n\pi}{W_x}$ denotes the wave number of the nth mode and $\omega_n = \sqrt{g \frac{n\pi}{W_x} \tanh\left(\frac{n\pi h_0}{W_x}\right)}$ represents the frequency of the nth mode. The wave period can be calculated by the leading wave mode ($n = 1$), hence $T = \dfrac{2\pi}{\omega_1} = 1.13391746$.

When M_c is between 15 and 35, the solution is unaffected by the amount of frequency components, according to Al-Tameemi et al. (2016) [13]. Hence, in this study, we select M_c as 25 for all simulations conducted. Accuracy is assessed by refining the time step Δt(steps per natural period T) and the number of free surface collocation points M_x. Convergence and rates are measured against the reference VSM solution (VSM$_r$) computed with 800 steps per T and $M_x = 160$. The VSM algorithm was implemented in Fortran 95 using double-precision arithmetic and modular procedures for modal summation, least-squares assembly, and Runge–Kutta time stepping. Numerical integrations for kinetic-energy diagnostics employed Romberg's method.

4.2. Free Surface Elevation

This part analyzes the numerical outcomes of the VSM water sloshing simulation by contrasting the free surface elevation at $x = W_x$ with the analytical solution 4.1. Furthermore, the convergence regarding the number of time steps per wave cycle and the resolution points M_x is examined.

The magnitude of the time step significantly influences the convergence of numerical models. The VSM technique is executed with 160 resolution points M_x along the free surface to examine the impact of this parameter on water sloshing models. Simulations are conducted with 50, 100, 200, 400, and 800 time steps per period.

At the simulation point ($x = W_x$), the free surface elevation for $\theta = 0.01, 0.05$, and 0.1 is compared with the linear analytical solutions presented in equations 4.1 in Figure 2. The VSM system utilizes two distinct time steps: $\Delta t/T = 1/50$ and $1/800$. The selected time steps for $\theta = 0.1$ are $\Delta t/T = 1/200$ and $1/800$. The VSM demonstrates that free surface elevation is consistent for both coarse and fine time increments. Conversely, when θ increases, the quantity of high-order nonlinear features escalates. Despite a substantial time step, the divergence between the first-order and VSM numerical outcomes is imperceptible when $\theta = 0.001$, as seen in Figure 2a. Figure 2b demonstrates that the VSM model, using a substantial time step ($\Delta t/T = 1/800$), exhibits a commendable connection with the first-order theoretical solution.

As θ grows beyond 0.05, the nonlinearity becomes more pronounced, leading to a divergence between the linearized analytical solution and the VSM results. This is attributable to the inadequacy of linear analytical solutions for modelling the behaviour of the extremely nonlinear free surface.

Figure 3 displays images of $\eta(x,t)$ throughout a typical cycle at the maximum tilt, $\theta = 0.1$. The spatial configuration is characterized by the primary standing-wave pattern, featuring antinodes adjacent to the lateral walls and a symmetry plane near the midpoint, in accordance with the antisymmetric tilt-and-release initial condition. In contrast to strictly linear theory, the profiles display anticipated weak-nonlinear characteristics, crest sharpening and moderate trough broadening, accompanied by a subtle setup/set-down bias throughout the cycle. The deformations represent the spatial equivalent of the amplitude-dependent frequency downshift observed in the wall time series in Figure 2 : the wave persists longer at extrema, manifested as flatter crests and gentler troughs.

To ascertain the estimated accuracy order of the existing VSM. Examine the l_2-norm of the error:

$$l_2 - Error = \sqrt{\frac{1}{n}\sum_{i=1}^{n}\left[\eta(W_x, t_i) - \eta_r(W_x, t_i)\right]^2}, \tag{4.2}$$

where the reference solution's elevation, denoted as η_r, is being compared. For the VSM$_r$ solution, Figure 4 shows the l_2-norm of the free surface elevation as a function of the number of time steps per wave period. The convergence rate of the scheme concerning temporal integration is established at fourth order, so validating the fourth-order accuracy of the Runge-Kutta numerical integration method. Furthermore, it is evident that the inaccuracy diminishes as the value of θ decreases.

To ascertain the convergence rate about M_x. We implement the VSM method using resolution points M_x of 40, 80, 160, and 320, and then utilize equation 4.2 for determining the convergence rate about M_x. The VSM approach's convergence rate regards to M_x exceeds first order, as shown in Figure 5. Also, as the tilt becomes less noticeable, the level of imprecision drops.

4.3. Conservation of Energy and Mass

According to Grilli et al. (1989) [10], accurately assessing the time-stepping precision of NWT models is done by comparing the volume error to the original volume as:

$$\epsilon(V) = \frac{Vol(t) - Vol_0}{Vol_0}, \tag{4.3}$$

The global volume at any particular moment is denoted as $Vol(t)$. on time t, with Vol_0 being the initial tank volume of water and,

$$Vol(t) = \int_{\Gamma} h(x,t)\, dx. \tag{4.4}$$

The total energy, which includes both kinetic and potential energy, is the unit of measurement for energy conservation. Here is the formula for kinetic energy:

$$KE(t) = \frac{1}{2}\rho \int_{FS} \varphi(\mathbf{x}, t).\nabla\varphi(\mathbf{x}, t).d\mathbf{s}, \tag{4.5}$$

where,

$$d\mathbf{s} = \begin{pmatrix} -dh/dx \\ 1 \end{pmatrix}. \tag{4.6}$$

Accordingly,

$$\begin{aligned} KE(t) &= \frac{1}{2}\rho \int_{FS} \varphi(\mathbf{x}, t)\left[-u\frac{\partial h(x,t)}{\partial x} + v\right] dx \\ &= \frac{1}{2}\rho \int \varphi(\mathbf{x}, t)\frac{\partial h(x,t)}{\partial t} dx. \end{aligned} \tag{4.7}$$

The expression for potential energy is,

$$PE(t) = \frac{1}{2}\rho g \int (h(x,t))^2 dx. \tag{4.8}$$

Analytically assessing the integrals (4.4) and (4.8) allows one to derive $Vol(t)$ and $PE(t)$ for the VSM, following the steps outlined in (3.14).

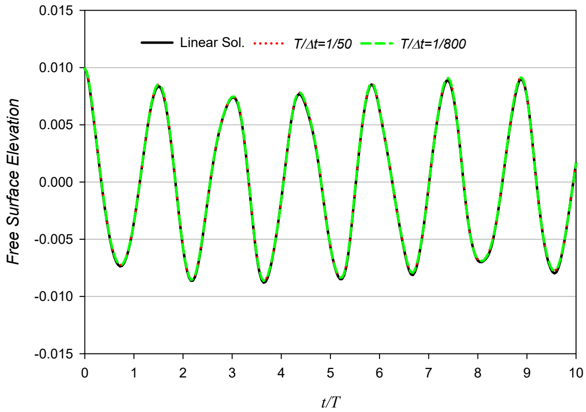

(a) $\theta = 0.01$

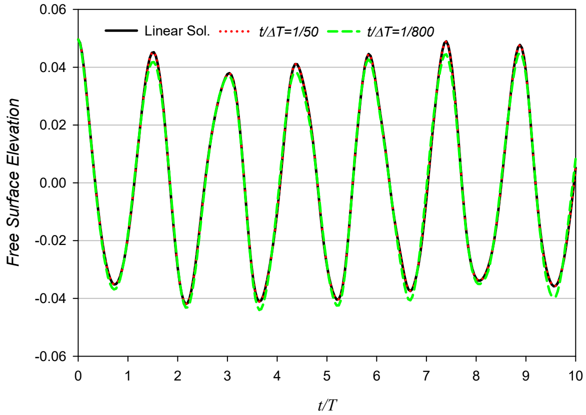

(b) $\theta = 0.05$

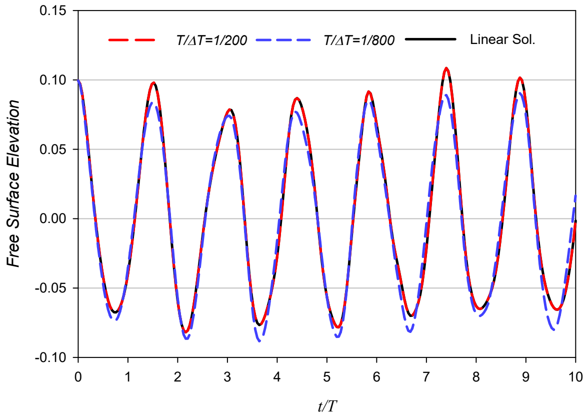

(c) $\theta = 0.1$

Figure 2: The evolution in free surface elevation over time at $x = W_x$ for W_x=1, h_0=1 with different values of θ and $T/\Delta t$

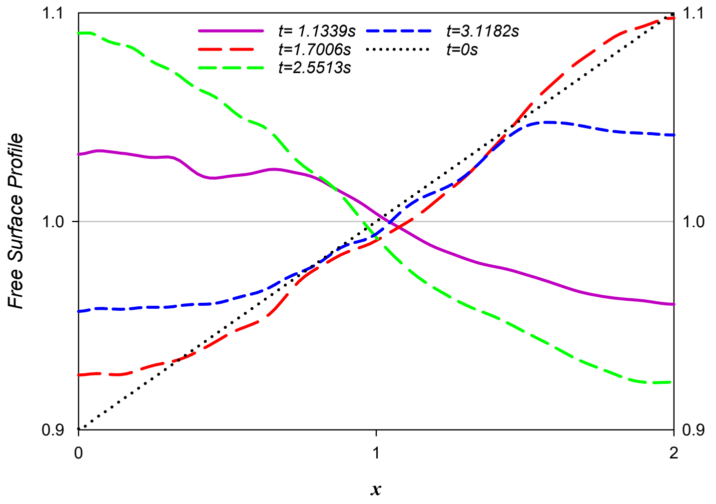

Figure 3: Free surface profiles at different time for $\theta = 0.1$.

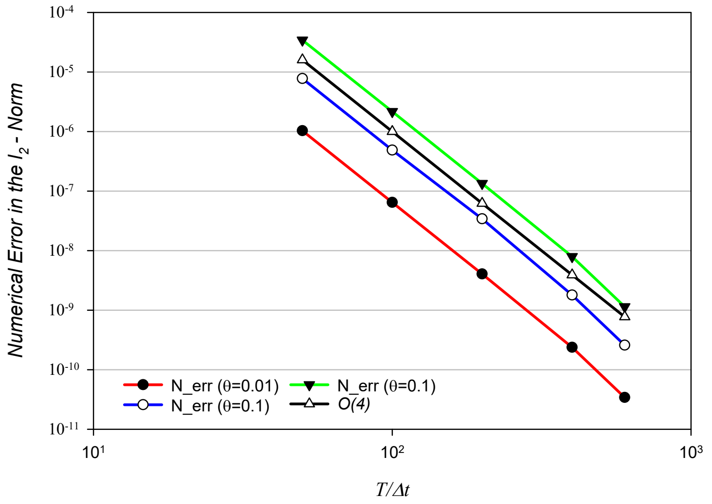

Figure 4: The l_2-norm of the free surface elevation differences between VSM solutions and VSM$_r$ for different tilts against $T/\Delta t$. in a log-log scale.

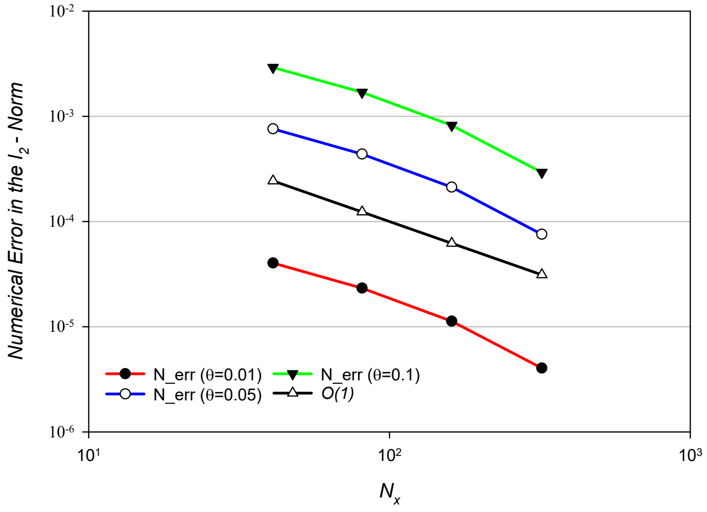

Figure 5: The l_2-norm of the free surface elevation differences between VSM solutions and the VSM$_r$ for different tilts against M_x in a log-log scale.

$$
\begin{aligned}
Vol(t) &= W_x H_z \int_0^1 \bar{h}(\bar{x},\bar{t})\, dx, \\
&= W_x H_z \int_0^1 \left(\sum_{k=0}^{N_A} [a_k(\bar{t}) \cos(\tfrac{2\pi}{W_x} k\, \bar{x}) + b_k(\bar{t}) \sin(\tfrac{2\pi}{W_x} k\, \bar{x})] \right).
\end{aligned}
$$

Therefore,

$$
Vol(t) = a_0(\bar{t}). \tag{4.9}
$$

PE(t) may also be written as

$$
PE(t) = \rho\, g\, H_z^2\, W_x \ \left((a_0(\bar{t}))^2 + \frac{1}{2} \sum_{k=1}^{N_A} \left[(a_k(\bar{t}))^2 + (b_k(\bar{t}))^2 \right] \right). \tag{4.10}
$$

The numerical solution to the equation (4.7) is used to obtain $KE(t)$ using Romberg's numerical integration method. .

The effects of increasing the number of time steps per period on the long-term conservation of energy and volume are shown in Figures 6-7. The total-energy drift $\epsilon(TE)$ (Figure 6) diminishes monotonically with an increase in the number of steps per fundamental period, resulting in bounded histories; at $\theta = 0.01$, the decay aligns with the effective order of the time integrator, whereas $\theta = 0.05$ and 0.1 exhibit marginally elevated baselines that converge with refinement. The volume error $\epsilon(V)$ (Figure 7) remains close to the numerical threshold across all examples, displaying only minimal, phase-locked oscillations that diminish consistently with decreasedΔt; no cumulative mass loss or gain is detected. The panels collectively demonstrate that over 50 steps per period are adequate for production precision across various tilts, whereas 80–100 steps per period significantly mitigate residual energy fluctuations in the most nonlinear scenario ($\theta = 0.1$). Refinement does not produce artificial damping or instability, highlighting the conservative nature of the VSM update and its mesh-free field assessment.

Figures 8 and 9 evaluate the impact of the number of free-surface collocation points M_x on long-term invariants at a constant, minimal time step (reference level). Figure 8 illustrates that augmenting M_x results in a consistently monotonic decrease in total-energy drift $\varepsilon_E(t)$ for all tilts $\theta \in \{0.01, 0.05, 0.1\}$. At coarse M_x, under-resolved wall-adjacent slopes—more prominent for bigger θ—appear as modest,

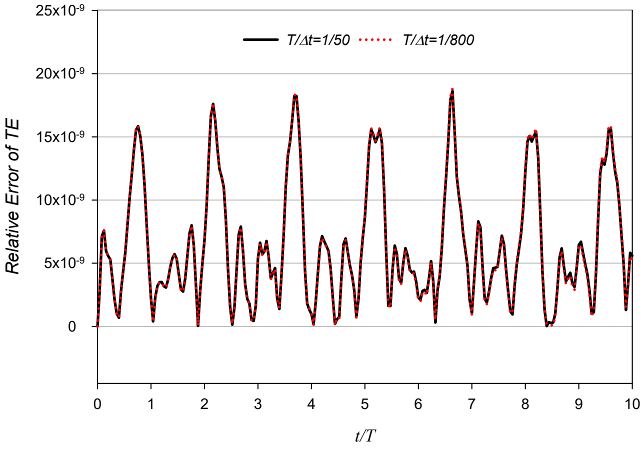

(a) $\theta = 0.01$

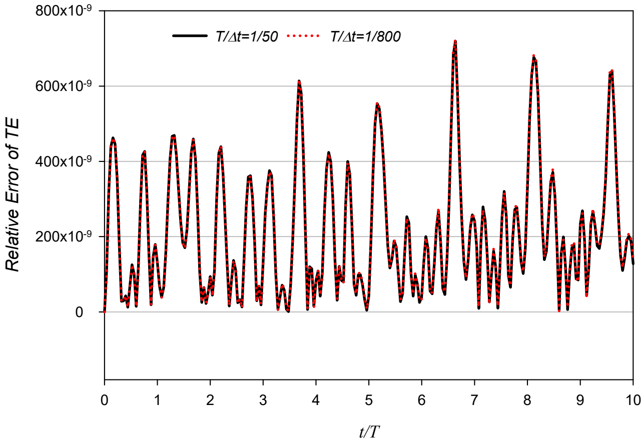

(b) $\theta = 0.05$

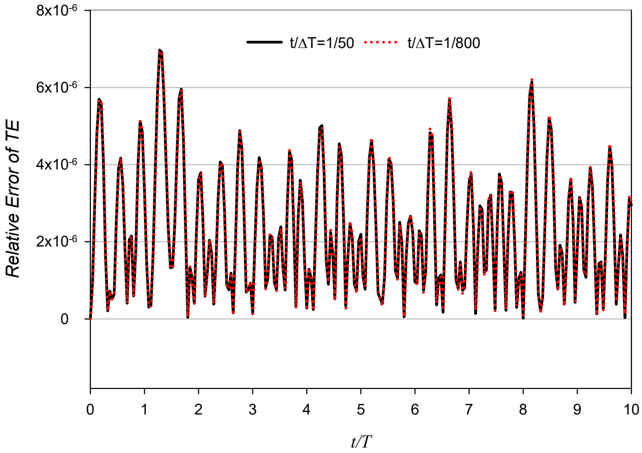

(c) $\theta = 0.1$

Figure 6: The relative error in total energy across different time steps per period as a function of time

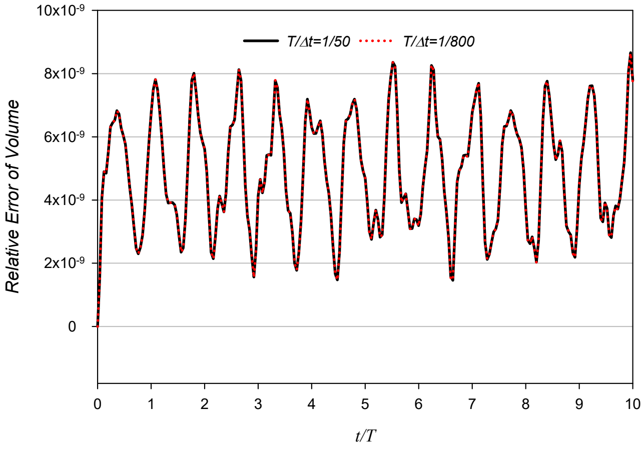

(a) $\theta = 0.01$

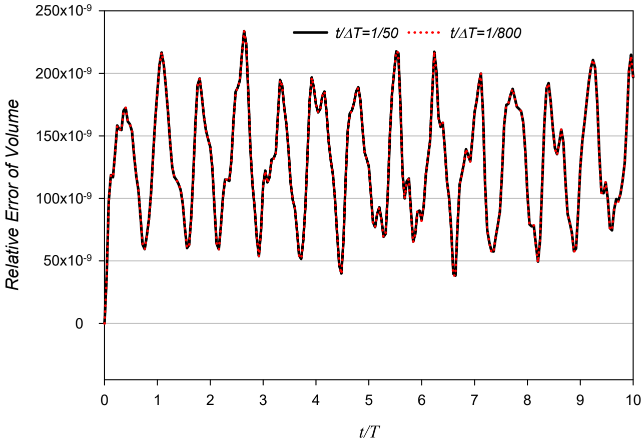

(b) $\theta = 0.05$

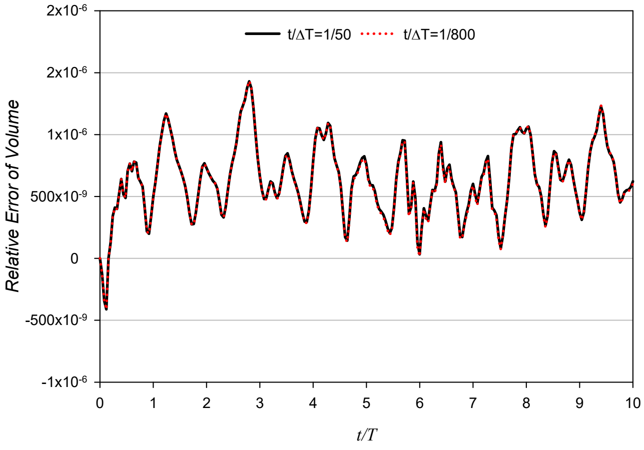

(c) $\theta = 0.1$

Figure 7: The relative error in total volume across different time steps per period as a function of time

persistent oscillations; these drop swiftly with refinement, resulting in bounded histories. Exceeding a problem-dependent threshold, additional increments in M_x result in declining returns, signifying that the error has reached the temporal limit established by Δt.

Figure 9 illustrates that volume conservation is consistently maintained across all M_x: the relative error $\varepsilon_V(t)$ remains close to the numerical threshold without any discernible trend, displaying only minor, phase-locked oscillations that diminish as M_x increases and subsequently stabilize at the same temporal limit. The panels collectively indicate that (i) energy serves as a more sensitive measure of spatial under-resolution—particularly for $\theta = 0.1$—and (ii) an effective approach is to select M_x sufficiently large to ensure that the spatial error aligns with the temporal error; beyond this threshold, further points yield minimal advantage.

Figures 10 and 11 illustrate the log–log temporal convergence of the long–time invariants in relation to $T/\Delta t$, utilizing the high–resolution VSM run (800 steps/period, $M_x = 160$, $M_c = 25$) as a benchmark. Figure 10 illustrates a strictly monotonic reduction of the overall energy error with temporal refinement for $\theta \in \{0.01, 0.05, 0.1\}$. At minimal tilt, the slope closely adheres to the effective order of the time integrator; with increased tilt, the slope is slightly diminished—aligned with steeper local gradients and heightened odd-harmonic content—yet saturation does not occur until the spatial limit (determined by M_x) is attained. Figure 11 demonstrates a markedly superior performance for mass: the relative volume error diminishes swiftly with increasing steps/period and promptly stabilizes at a minimal level, indicating near-machine conservation as temporal error becomes negligible. The panels collectively validate the insights derived from the time-history plots (Figs. 6–7): choosing $\gtrsim 50$ steps per period ensures adequate production accuracy across tilts, whereas 80–100 steps per period effectively confine the energy error within the temporal-plateau regime, even at $\theta = 0.1$.

At the largest tilt amplitude ($\theta = 0.1$), energy variations serve as a more sensitive diagnostic than volume conservation, because nonlinear interactions and sharper free-surface gradients amplify small numerical phase and amplitude errors, even though the overall fluid volume remains nearly invariant.

Figures 12 and 13 illustrate the log-log spatial convergence of the long-time invariants in relation to the number of free-surface collocation points M_x, at a constant, minimal time step. In Figure 12, the total energy error diminishes monotonically with M_x and demonstrates a distinct second-order rate in the pre-asymptotic regime: the fitted slope is $p \simeq 2$ for all tilts, with a slight reduction observed only at the largest amplitude due to steeper gradients adjacent to the wall. When M_x reaches a sufficient magnitude such that the spatial inaccuracy aligns with the temporal threshold established by Δt, the curves stabilize as anticipated. Figure 13 illustrates a similar trend for mass: the volume error diminishes predominantly at order two until it attains a minimal plateau dictated by temporal resolution and roundoff. Collectively, the panels suggest that—despite the spectral assessment of the internal field—the global invariants are governed by a second-order surface discretization/diagnostics approach; thus, a pragmatic sizing guideline is to augment M_x until the M_x^{-2} trend initially intersects the temporal plateau for the selected Δt.

5. Conclusion

This study examines the two-dimensional sloshing in a stationary rectangular tank induced by a tilt-and-release condition. The VSM was developed within a succinct eigenfunction framework, incorporating a closed-form vertical kernel and a compact least-squares system for the modal time derivatives. We performed simulations for a typical geometry (usually $W_x = 2$ m, $H_z = 1.5$ m, $h_0 = 1$ m) with a moderate and fixed virtual-mode count of $M_c = 25$ and three tilt amplitudes of $\theta \in \{0.01, 0.05, 0.1\}$. A high-resolution reference (800 steps per period, $M_x = 160$, $M_c = 25$) was used to check for accuracy and stability. Additional tests were done at $W_x = 1$ m, $h_0 = 1$ m for wall-trace diagnostics.

The results demonstrate *monotone* convergence of the free-surface elevation to the reference with both temporal and spatial refinement. With a sufficiently large M_x, temporal errors diminish at rates aligned with the effective order of the time integrator in the weakly nonlinear regime, but spatial refinement at a minimal time step yields a clean decrease in elevation norms until the temporal threshold is attained. The spatial profiles show the predicted weak–nonlinear signs with greater tilt: crest sharpening, modest trough broadening, and a minor amplitude–dependent downshift. These are caused by the odd–harmonic dominance of the antisymmetric tilt initial condition.

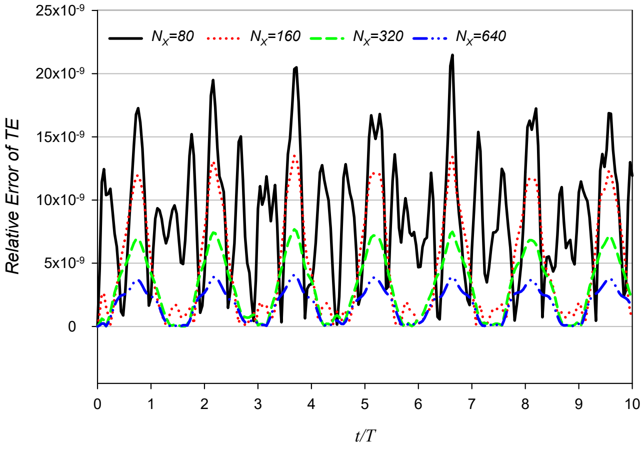

(a) $\theta = 0.01$

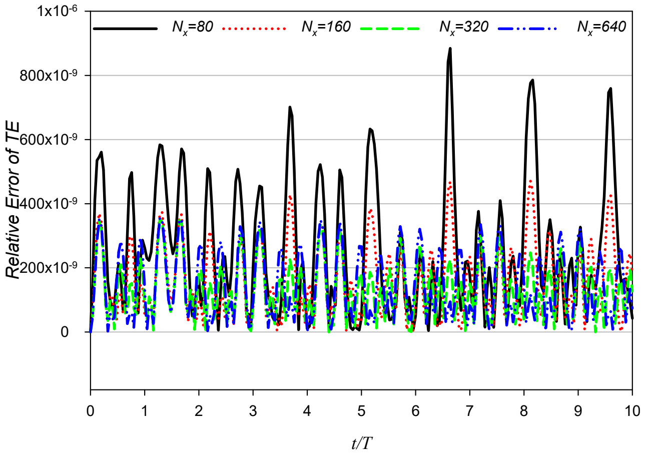

(b) $\theta = 0.05$

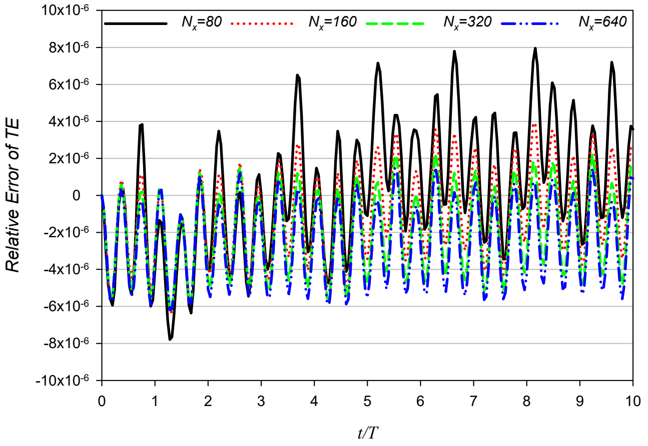

(c) $\theta = 0.1$

Figure 8: Temporal development of the relative error in total energy across various resolution points.

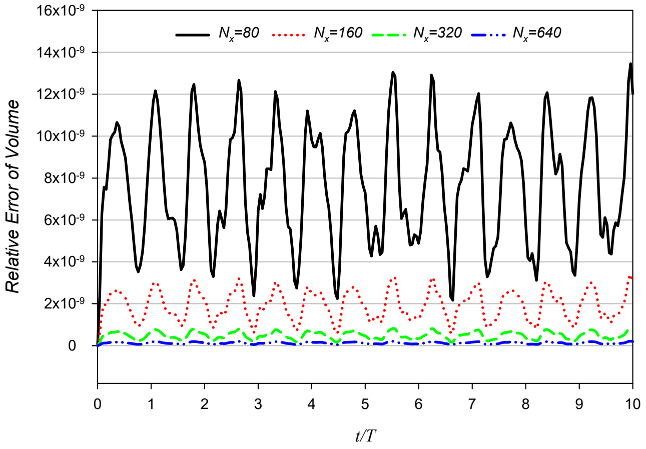

(a) $\theta = 0.01$

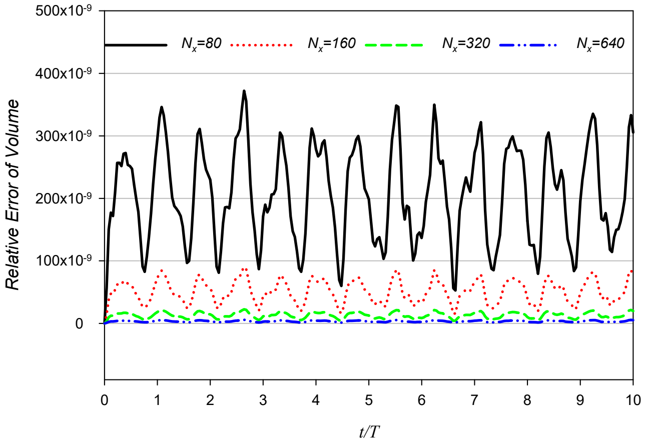

(b) $\theta = 0.05$

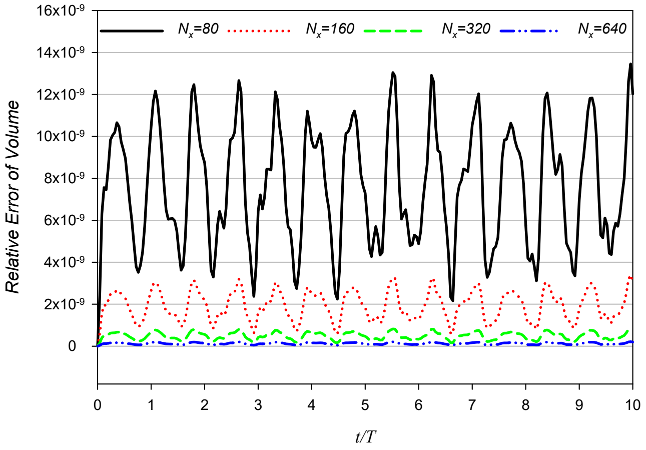

(c) $\theta = 0.1$

Figure 9: Temporal development of the relative error in total volume across various resolution points.

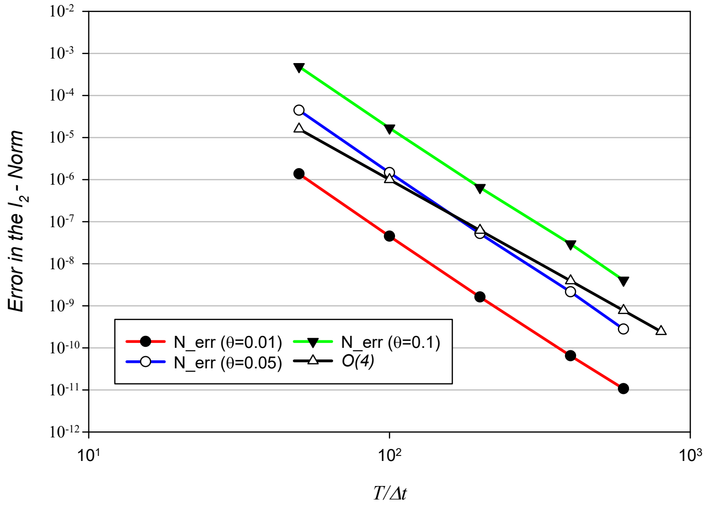

Figure 10: The l_2-norm of errors between VSM solutions and initial energy for different tilts versus $T/\Delta t$ on a log-log scale.

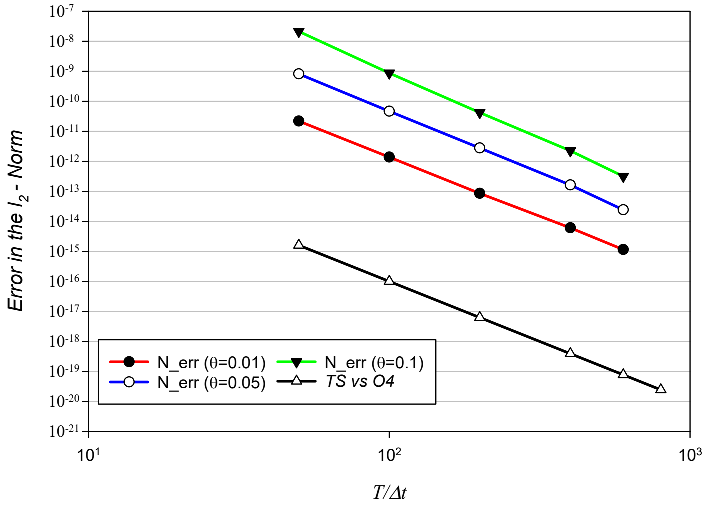

Figure 11: The l_2-norm of errors between VSM solutions and initial volume for different tilts versus $T/\Delta t$ on a log-log scale.

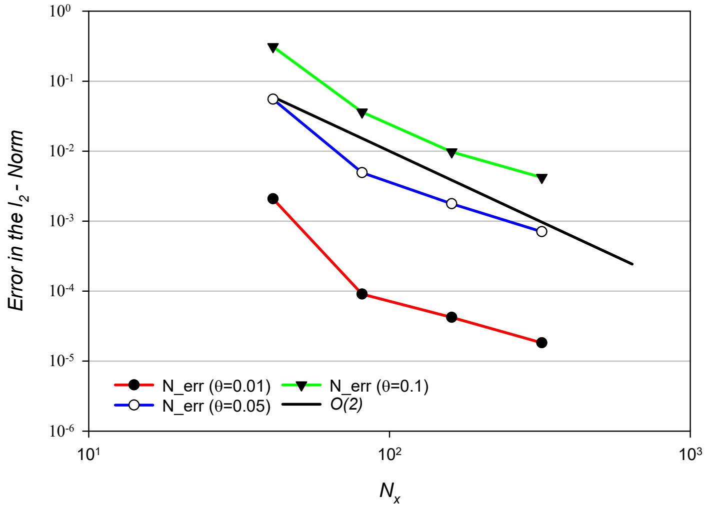

Figure 12: The l_2-norm of errors between VSM solutions and initial energy for different tilts versus M_x on a log-log scale.

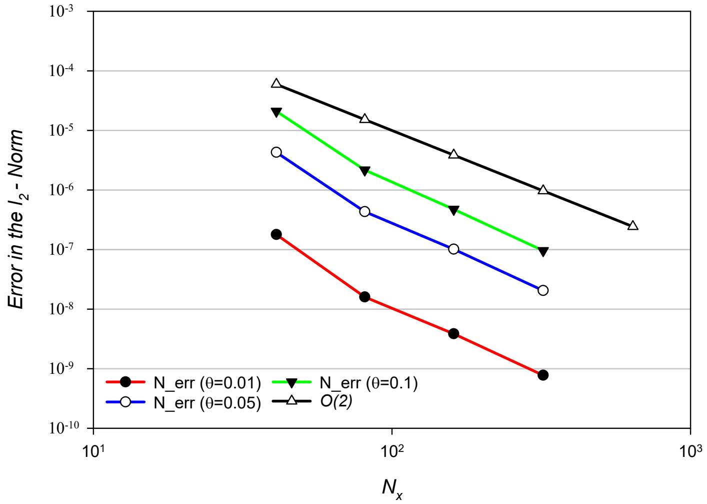

Figure 13: The l_2-norm of errors between VSM solutions and initial volume for different tilts versus M_x on a log-log scale.

Global diagnostics verify the formulation's conservative nature. The volume (mass) stays almost the same in all settings, with only small, phase-locked oscillations that get smaller as the settings get better. Over lengthy integrations, the total energy drift stays small, limited, and non-secular. It goes down in a predictable way when either the time stepping is finer or the free-surface resolution is higher. In log-log form, the invariants show a clear second-order spatial convergence before leveling out at the temporal limit. Energy is more sensitive to under-resolution than volume, especially at $\theta = 0.1$.

The study provides straightforward suggestions for practical application. Using at least 50 time steps each fundamental period gives you high-quality wall traces, accurate profiles, and histories that don't change with different tilts. For the most nonlinear situation ($\theta = 0.1$), 80–100 steps per period reduce residual phase and energy wiggles even more. The free-surface collocation should be raised until the spatial error meets (but doesn't go too far below) the temporal floor; beyond that, returns start to drop. It works to keep M_c at a reasonable level (around 25) because accuracy is determined by Δt and M_x after the vertical series has converged.

The current investigation is inviscid, irrotational, and two-dimensional, hence omitting viscous dissipation, air cushioning, and impact or fragmentation phenomena. Future endeavors will advance VSM into three dimensions, integrate dissipative and subgrid impact models, and connect with structural dynamics to facilitate fluid-structure interaction during extreme sloshing events. The VSM provides precise, stable, and efficient long-term forecasts for rectangular-tank sloshing, featuring transparent resolution controls and verifiable convergence to a reliable reference.

References

1. O. M. Faltinsen, A. N. Timokha, *Sloshing*, Cambridge Univ. Press, (2009).
2. O. M. Faltinsen, O. F. Rognebakke, I. A. Lukovsky, A. N. Timokha, *multidimensional modal analysis of nonlinear sloshing in a rectangular tank with finite water depth*, J. Fluid Mech., 407, 201–234, (2000).
3. C. W. Hirt, B. D. Nichols, *volume of fluid (vof) method for the dynamics of free boundaries*, J. Comput. Phys., 39, No. 1, 201–225, (1981).
4. S. J. Cummins, M. Rudman, P. W. Cleary, *sph simulation of wave–structure interaction*, Coastal Eng., 36, No. 3, 223–239, (1999).
5. S. Koshizuka, Y. Oka, *moving-particle semi-implicit method for fragmentation of incompressible fluid*, Nucl. Sci. Eng., 123, No. 3, 421–434, (1998).
6. H. Li, X. Zhang, X. Yang, *numerical study of liquid sloshing using smoothed particle hydrodynamics with adaptive spatial resolution*, Engrg. Anal. Bound. Elem., 159, 272–287, (2024).
7. W. Bai, R. E. Taylor, *numerical modelling of violent free-surface flows*, J. Hydrodyn., 19, No. 3, 378–386, (2007).
8. W. Bai, C. G. Mingham, D. M. Causon, *finite volume simulation of viscous free surface waves using the cartesian cut cell approach*, Int. J. Numer. Methods Fluids, 63, No. 1, 69–95, (2010).
9. G. Wu, R. E. Taylor, *finite element analysis of two-dimensional non-linear transient water waves*, Appl. Ocean Res., 16, No. 6, 363–372, (1994).
10. S. T. Grilli, J. Skourup, I. A. Svendsen, *an efficient boundary element method for nonlinear water waves*, Engrg. Anal. Bound. Elem., 6, No. 2, 97–107, (1989).
11. S. T. Grilli, P. Guyenne, F. Dias, *a fully non-linear model for three-dimensional overturning waves over an arbitrary bottom*, Int. J. Numer. Methods Fluids, 35, No. 7, 829–867, (2001).
12. K. Langfeld, D. I. Graham, D. M. Greaves, A. Mehmood, T. Reis, *the virtual source approach to non-linear potential flow simulation*, Proc. 26th Int. Offshore Polar Engrg. Conf. (ISOPE), Rhodes, Greece, (2016).
13. O. Al-Tameemi, D. I. Graham, K. Langfeld, *accuracy and stability of virtual source method for numerical simulations of nonlinear water waves*, Proc. 28th Int. Offshore Polar Engrg. Conf. (ISOPE), Sapporo, Japan, (2018).
14. O. Al-Tameemi, D. I. Graham, K. Langfeld, *virtual source method simulation of progressive water waves*, Proc. 29th Int. Offshore Polar Engrg. Conf. (ISOPE), Honolulu, USA, (2019).
15. M. S. Longuet-Higgins, E. D. Cokelet, *the deformation of steep surface waves on water. i. a numerical method of computation*, Proc. R. Soc. Lond. Ser. A, 350, No. 1660, 1–26, (1976).
16. T. J. Thomas, G. S. Dwarakish, *numerical wave modelling – a review*, Aquat. Procedia, 4, 443–448, (2015).
17. P. Lin, C. W. Li, *a ζ-coordinate three-dimensional numerical model for surface wave propagation*, Int. J. Numer. Methods Fluids, 38, No. 11, 1045–1068, (2002).
18. A. Bardazzi, C. Lugni, O. M. Faltinsen, D. Durante, A. Colagrossi, L. D'Agostino, *Different scenarios in sloshing flows near the critical filling depth*, J. Fluid Mech., 984, A73, (2024).

19. Xin Jin, Hua-long Huang, Yi-yi Qin, Hao Yang, Fu-gui Zhang, *Slosh transient variations in rectangular tanks under oblique excitations*, Phys. Fluids, 36(10), (2024).
20. P.Peng, , Z. Gao, X. Li, K. Liu, *Experimental study of sloshing flows in a rectangular tank under coupled pitch and heave excitations*, Ocean Eng., 309, 118544, (2024).
21. H. Li, X. Zhang, and X. Yang, *Numerical study of liquid sloshing using smoothed particle hydrodynamics with adaptive spatial resolution*, Eng. Anal. Bound. Elem., 159, 272–287, (2024).
22. T. Konar, P. Mandal, S. Chakraborty, *A review of numerical modelling of liquid sloshing in partially filled tanks*, Ships Offshore Struct., 1–16(2025).

Omar Al-Tameemi,
Department of Mathematics and Computer Applications,
College of Sciences,
Al-Nahrain University,
Jadriya, Baghdad, Iraq.
E-mail address: `omar.ismael@nahrainuniv.edu.iq`

and

A. Al-Sabbagh,
Department of Mathematics and Computer Applications,
College of Sciences,
Al-Nahrain University,
Jadriya, Baghdad, Iraq.
E-mail address: `akram.alsabbagh@nahrainuniv.edu.iq`

and

Ruaa Wana,
Studies Planning and Follow-Up Directorate,
Ministry of Higher Education and Scientific Research,
Baghdad,
Iraq.
E-mail address: `ruaawana@mohesr.edu.iq`

and

Aqeel Jassim Noor,
Department of Mathematics,
University of Wasit,
Wasit, Iraq.
E-mail address: `aqeel.noor@uowasit.edu.iq`